buildings

MDPI

Article

The Mechanical Properties and Durability of the PE-BFRP Hybrid-Fiber-Engineered Cementitious Composite (ECC)

Shasha Xu [1], Wei Li [1], Xuezhen Wang [1], Hongze Zhang [1], Ju Liu [1], Hui Jiang [1], Xuebin Wang [1], Hongke Ma [2], Jun Shi [3], Zhenyun Yu [2] and Kuangyu Dai [2,*]

[1] SINO-SINA Building Materials Co., Ltd., Zhengzhou 452370, China; songsongshasha1234@163.com (S.X.); 13920472056@163.com (W.L.); 13488781841@126.com (X.W.); 15039786981@163.com (H.Z.); m15538310015@163.com (J.L.); 15537117175@163.com (H.J.); wangxuebin@xauat.edu.cn (X.W.)
[2] School of Civil Engineering, Zhengzhou University, Zhengzhou 450001, China; 13781978696@163.com (H.M.); yuzhenyun@zzu.edu.cn (Z.Y.)
[3] School of Civil Engineering, Central South University, Changsha 410083, China; csushijun@csu.edu.cn
* Correspondence: daikuangyu@zzu.edu.cn

Abstract: This paper investigates the effects of the basalt-fiber-reinforced polymer (BFRP) and polyethylene (PE) hybrid fiber ratio on the mechanical properties and durability of engineered cementitious composites (ECC). First, four different PE-BFRP hybrid fiber ECC mixtures were systematically prepared by controlling the fiber volume ratio of PE and BFRP fibers. The workability and mechanical properties of the hybrid fiber ECC (HFECC) were then evaluated using flowability tests and multi-scale mechanical tests, including compressive strength, flexural strength, bending toughness, and tensile performance. After that, the durability of HFECC with different fiber ratios was comprehensively assessed through freeze–thaw cycle tests and rapid ion migration tests. Finally, the interface morphology of fibers within the matrix was observed using scanning electron microscopy (SEM). The results show that an appropriate hybrid of PE and BFRP fibers can synergistically enhance the crack resistance and toughness of ECC, improving its failure mode. The best performance in terms of flowability and mechanical properties was observed for the HFECC mixture with 1.30% PE fiber volume and 0.30% BFRP fiber volume. With the increase in BFRP fiber content, the freeze–thaw resistance and chloride ion erosion resistance of HFECC were gradually enhanced. This study provides experimental and theoretical support for the design and engineering application of high-performance hybrid fiber ECC materials.

Keywords: PE-BFRP hybrid fiber; engineered cementitious composite; mechanical properties; freeze–thaw cycle; chloride ion penetration

check for updates

Academic Editor: Eugeniusz Koda

Received: 24 April 2025
Revised: 16 May 2025
Accepted: 20 May 2025
Published: 28 May 2025

Citation: Xu, S.; Li, W.; Wang, X.; Zhang, H.; Liu, J.; Jiang, H.; Wang, X.; Ma, H.; Shi, J.; Yu, Z.; et al. The Mechanical Properties and Durability of the PE-BFRP Hybrid-Fiber-Engineered Cementitious Composite (ECC). *Buildings* **2025**, *15*, 1860. https://doi.org/10.3390/buildings15111860

Copyright: © 2025 by the authors. Licensee MDPI, Basel, Switzerland. This article is an open access article distributed under the terms and conditions of the Creative Commons Attribution (CC BY) license (https://creativecommons.org/licenses/by/4.0/).

1. Introduction

An engineered cementitious composite (ECC) is a type of high-performance fiber-reinforced cementitious material designed based on micromechanics that exhibits significant strain-hardening behavior and multiple crack patterns [1,2]. The ultimate tensile strain of ECC can exceed 3%, much higher than that of ordinary concrete, which is typically between 0.01% and 0.05% [3]. Unlike traditional concrete, ECC forms numerous fine, closely distributed microcracks (usually less than 100 μm in width) under loading, rather than a single macrocrack, significantly enhancing the material's toughness and durability [4]. Additionally, ECC has excellent crack self-healing ability in humid environments, further extending the service life of structures [5]. Due to its excellent mechanical properties and durability, ECC has been widely applied in seismic structures, bridge panel repair, and building retrofitting [6].

The performance of ECC is highly dependent on the characteristics of the fibers used. Currently, single-fiber-reinforced ECC systems, such as those with Polyvinyl Alcohol (PVA) fibers, polyethylene (PE) fibers, Polypropylene (PP) fibers, or steel fibers [7–10], have shown significant advantages in specific applications. However, due to the inherent physical and chemical properties of the fibers, their overall performance still has evident limitations. For instance, PVA-fiber-reinforced ECC achieves significant strain-hardening effects and multiple-cracking behavior. The tensile strains can reach 3–5% for PVA-reinforced ECC [11]. However, the poor water resistance of PVA fibers leads to interface degradation in humid environments, severely affecting the long-term durability of the material [12]. Steel-fiber-reinforced ECC significantly enhances compressive strength and elastic modulus [13,14]. However, the deformation capacity of steel-fiber-based ECC is usually less than 1%. This fails to meet the fundamental requirement for high ductility in ECC. In contrast, PE fibers exhibit excellent chemical corrosion resistance and ductility (with breaking elongation exceeding 3%). However, their low elastic modulus leads to insufficient early stiffness in PE-fiber-based ECC. This poses a risk of excessive deformation in structural applications [15,16].

In recent years, hybrid-fiber-reinforced ECC (HFECC) has gained attention. By combining fibers with complementary advantages, it is possible to optimize both the mechanical properties and the durability of the material. For example, Liu et al. [13] studied the hybrid steel–PVA fiber system and found that the hybrid fiber mixture improved both compressive strength and tensile ductility compared to using a single fiber. Huo et al. [14] also studied steel/PE hybrid fiber HFECC and found that the mixed fibers enhanced dynamic tensile properties, with the failure mode of PE fibers changing from rupture to pull-out. Wang et al. [17] found that steel and PVA fiber HFECC showed an increase in flexural strength by 9.3–34.3% and toughness by 42–47% when the PVA fiber volume fraction ranged from 0.25% to 0.75%. Hou and Li [18] hybridized PP fibers with PVA fibers. They achieved a crack width of only 50 μm at a tensile strain of 2%. Ahemd et al. [19] found through four-point bending tests that the highest flexural strength occurred with a mixture of 1.5% PE fibers and 1.0% steel fibers, while the strongest deformation performance was observed with 2.0% PE fibers and 0.5% steel fibers. Zhou et al. [20] found that the flexural strength and deflection of PE and steel fiber hybrid HFECC increased with the PE fiber content, while the flexural strength decreased with increasing steel fiber content. Tinoco et al. [21] also used PE fibers and steel fibers in a hybrid system. They found that the crack width increased with the addition of steel fibers. With increasing steel fiber content, the crack width decreased, but the crack spacing increased. Existing research mainly focuses on hybrid systems of steel fibers, PVA fibers, and PE fibers. The synergistic effects of other high-performance fibers, such as basalt-fiber-reinforced polymer (BFRP) fibers, in hybrid systems remain insufficiently explored.

BFRP is a novel inorganic fiber. It offers high strength, high elastic modulus, excellent alkali resistance, and high-temperature performance [22]. It is also more cost-effective than carbon fibers. Recent studies have also explored the effects of incorporating basalt fibers into various cementitious systems. Dias et al. [23] found that basalt-fiber-reinforced geopolymer cement concrete exhibited improved flexural strength, tensile strength, and fracture toughness, primarily due to fiber debonding, sliding, and pull-out mechanisms. Branston et al. [24] reported that basalt fibers enhanced the pre-crack strength of concrete and contributed to improved post-crack behavior through effective bridging and pull-out. However, other studies have pointed out potential drawbacks. Ayub et al. [25] and Zhou et al. [26] noted that basalt fibers could negatively affect the workability and compressive strength of the composite. Regarding durability, Wang [27] demonstrated that a moderate dosage of basalt fibers enhanced the frost resistance of cement-based materials. Nonetheless,

excessive fiber content led to overlapping effects that hindered freeze–thaw performance. Wang et al. [28] and Liu [29] further observed that, when the basalt fiber volume content was limited to 0.1%, the composites exhibited the lowest ion permeability and the highest acid corrosion resistance. According to the previous studies, introducing BFRP into the ECC system may compensate for the low elastic modulus of PE fibers. This can improve the material's early stiffness and compressive strength. Meanwhile, the ultra-high ductility and chemical corrosion resistance of PE fibers ensure that ECC maintains excellent strain-hardening behavior during the crack-development phase. Theoretically, a PE-BFRP hybrid fiber ECC could combine high stiffness, high strength, and high ductility. It would also provide excellent durability, making it suitable for structural applications in corrosive environments (e.g., marine engineering and chemical plant structures). However, there is currently very limited research on PE-BFRP hybrid fiber ECC. The synergistic mechanisms between the two fibers, the optimal hybrid ratio, and their effects on long-term durability have not been fully explored.

In light of this, the present study investigates the mechanical and durability properties of HFECC with PE fibers as the primary reinforcement and BFRP fibers as secondary reinforcement. First, HFECC specimens are systematically prepared by adjusting the fiber volume ratio between PE fibers and BFRP fibers. Next, the mechanical properties of PE-BFRP hybrid ECC materials are comprehensively characterized through flowability tests and multi-scale mechanical performance tests, including compressive strength, three-point flexural strength, four-point equivalent bending strength and toughness strength, and tensile strength tests. Subsequently, the durability of HFECC materials with different fiber ratios is evaluated through freeze–thaw cycle tests and chloride ion penetration tests. Finally, scanning electron microscopy (SEM) is used to reveal the fiber–matrix interface bonding mechanisms and the synergistic working mechanisms of PE and BFRP fibers within the cementitious matrix. This study provides theoretical and technical support for the material design and engineering applications of HFECC.

2. Materials and Experimental Setup

The raw materials for the preparation of HFECC include the following: (1) ordinary Portland cement (P.O 42.5) with a loss on ignition (LOI) of 1.238%; (2) fly ash with a LOI of 2.3%; (3) SF90 silica fume with a LOI of 1.85%; (4) quartz sand with an average particle size range of 0.09 mm to 0.12 mm and a maximum particle size of 0.15 mm; (5) a high-efficiency polycarboxylate-based superplasticizer with a water reduction rate $\geq$ 25%; (6) ordinary tap water; (7) PE fibers of 12 mm in length; and (8) BFRP fibers of 15 mm in length. It is worth noting that the P.O 42.5 cement used in this study complies with the Chinese standard GB 175-2007 [30], which classifies cement primarily based on compressive strength at 28 days. This type is roughly equivalent to ASTM C150 [31] Type I Portland cement commonly used in the United States and CEM I under EN 197-1 [32] in Europe. The primary raw materials are shown in Figure 1. The performance specifications of the fibers are presented in Table 1.

Table 1. Physical and mechanical properties of PE and BFRP fibers.

Material	Density (g/cm^3)	Diameter (μm)	Tensile Strength (GPa)	Elastic Modulus (GPa)	Elongation at Break (%)
PE Fiber	0.97	16	4.4	65	3.5
BFRP fiber	2.63	17	3.66	110	3.1

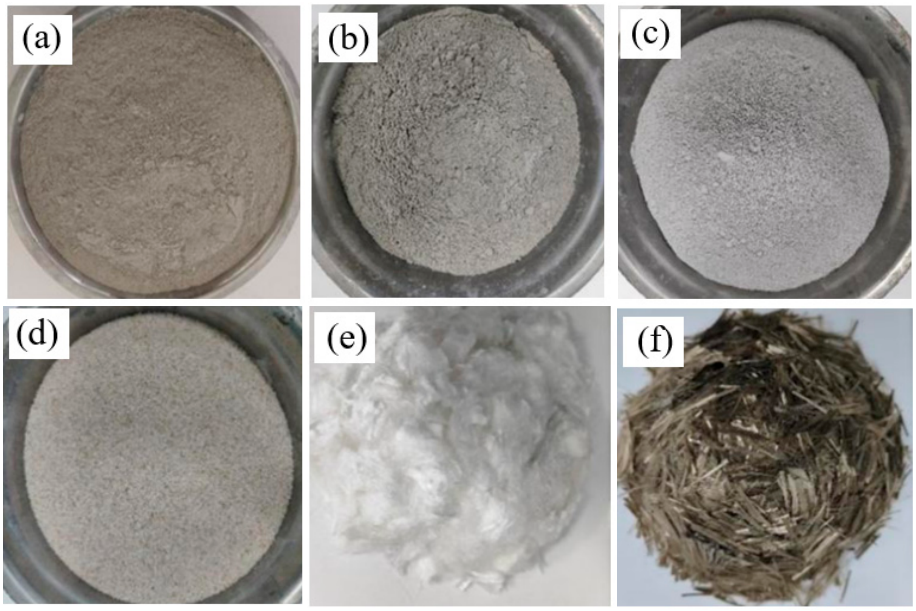


Figure 1. Main raw materials for HFECC: (**a**) cement; (**b**) fly ash; (**c**) silica fume; (**d**) quartz sand; (**e**) PE fibers; (**f**) BFRP fibers.

The matrix material mix was optimized with a ratio of cement:fly ash:silica fume:quartz sand:water = 1:0.78:0.18:0.66:0.39 by mass. The dosage of polycarboxylate superplasticizer was fixed at 0.20% of the total mass of the binder materials. The total fiber volume ratio of hybrid fibers was optimized at 1.6%. This was achieved by adjusting the volume content of PE and BFRP fibers. The adjustment was based on fresh mixture workability tests and mechanical performance optimization. Preliminary experiments were conducted to evaluate the workability and fiber dispersion of the mixtures. The results indicated that higher dosages of BFRP fibers, due to their rough surface texture, adversely affected the slurry's cohesion and fiber dispersion, leading to poor workability. Furthermore, it was found that a higher proportion of PE fibers was essential to maintain good workability, as PE fibers improve the flowability and cohesion of the mixture. Based on these preliminary findings, the fiber volume ratio of 1.6% was chosen, balancing both workability and mechanical performance. Four HFECC mix ratio schemes were designed, as follows: (1) HFECC-1: PE fiber 1.40 vol.% + BFRP fiber 0.20 vol.%; (2) HFECC-2: PE fiber 1.35 vol.% + BFRP fiber 0.25 vol.%; (3) HFECC-3: PE fiber 1.30 vol.% + BFRP fiber 0.30 vol.%; and (4) HFECC-4: PE fiber 1.25 vol.% + BFRP fiber 0.35 vol.%. Subsequently, flowability tests and compressive strength, three-point flexural strength, four-point equivalent bending strength and toughness strength, and tensile strength tests were conducted on the four sets of specimens.

For the flowability test, the jump table method was used to determine the flowability of each HFECC group according to the GB/T 2419-2005 "Test method for fluidity of cement mortar" [33]. The entire test process was conducted in a constant temperature and humidity environment (20 ± 2 °C, relative humidity $\geq 50\%$). After the HFECC was evenly mixed using a planetary mortar mixer, the prepared mortar was placed in a truncated cone mold with an upper diameter of 70 mm, a lower diameter of 100 mm, and a height of 60 mm (as shown in Figure 2). The mortar was filled in two layers, each layer was compacted 15 times vertically with a standard 20 mm diameter tamping rod, and the surface of the mold was then leveled. After removing the mold, the standard jump table device was activated, completing 25 jumps with an amplitude of 25 ± 1 mm and a frequency of 1 Hz. The flowability of the material was then determined.

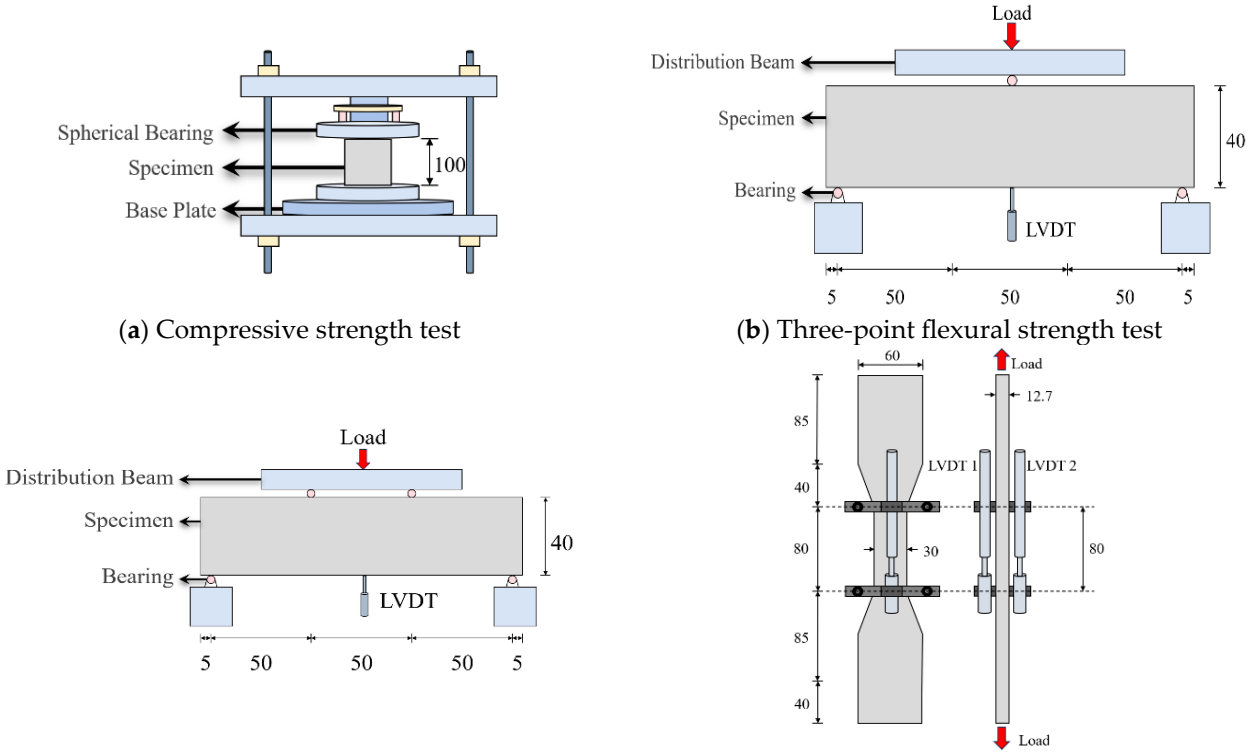


Figure 2. Flowability test equipment and method.

A series of mechanical performance tests were conducted in accordance with China's current standards and specifications. The compressive strength test followed the GB/T 50081-2019 "Standard for test methods of concrete physical and mechanical properties" [34]. The 100 mm cubic specimens were used for axial compression testing on a universal testing machine, as shown in Figure 3a. The loading rate was 0.5 MPa/s. Each group contained three specimens. In accordance with the standard, the compressive strength of each group was determined by calculating the arithmetic mean of the three measured values, accurate to 0.1 MPa. If either the maximum or minimum value differed from the median by more than 15%, both outliers were excluded, and the median was taken as the final result. If both the maximum and minimum values deviated by more than 15% from the median, the test results for that group were considered invalid. The three-point flexural strength test followed the GB/T 17671-2021 "Method for testing the strength of cement mortar (ISO method)" [35]. The 40 mm × 40 mm × 160 mm prismatic specimens were used. The test applied a three-point bending loading regime with a span of 100 mm. The loading rate was 50 N/s. Each group consisted of three specimens. According to the standard, the average of the three results was taken as the final flexural strength. If one of the three values deviated from the average by more than ±10%, it was discarded, and the average of the remaining two was used. If two of the three values deviated by more than ±10% from the average, only the remaining valid value was taken as the final result. The specimen specifications are shown in Figure 3b. The equivalent bending strength and toughness were determined according to the DBJ41/T 236-2020 "Technical standard for strengthening rural buildings with high ductility concrete" [36]. The 40 mm × 40 mm × 160 mm prismatic specimens were used for four-point bending tests [37]. The pure bending segment length was 50 mm. Each group consisted of three specimens. The loading rate was displacement-controlled at 0.2 mm/min. The test setup is shown in Figure 3c. After completing the four-point bending test loading, the equivalent bending strength ${f_{eq}}^{u}$ and equivalent bending toughness ${W_c}^{u}$ of the specimens were calculated. The calculation method for the equivalent bending strength and equivalent bending toughness followed the same statistical criteria as the flexural strength test. The equivalent bending strength was calculated as shown in Figure 4 and Equation (1).

$$f_{eq}^{u} = \frac{\Omega_u L}{bh^2 \delta_u} \quad (1)$$

where, ${f_{eq}}^{u}$ is the equivalent bending strength (N/mm^2), accurate to 0.1 N/mm^2; Ω_u is the area under the load–deflection curve at mid-span deflection δ_u (N·mm); δ_u is the deflection corresponding to a load drop to u times the peak load, where u = 0.85 in this study; b and h are the specimen's cross-sectional width and height (mm); and L is the span of the specimen (mm).



(**a**) Compressive strength test

(**b**) Three-point flexural strength test

(**c**) Four-point equivalent bending strength and toughness test

(**d**) Tensile strength test

Figure 3. Geometry and loading boundary conditions of the mechanical performance test specimens.

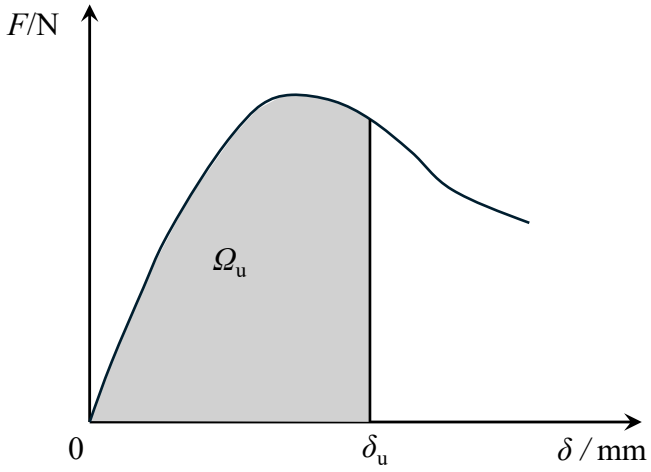


Figure 4. Schematic of equivalent bending toughness calculation.

The equivalent bending toughness $W_c{}^u$ was calculated using Equation (2), as follows:

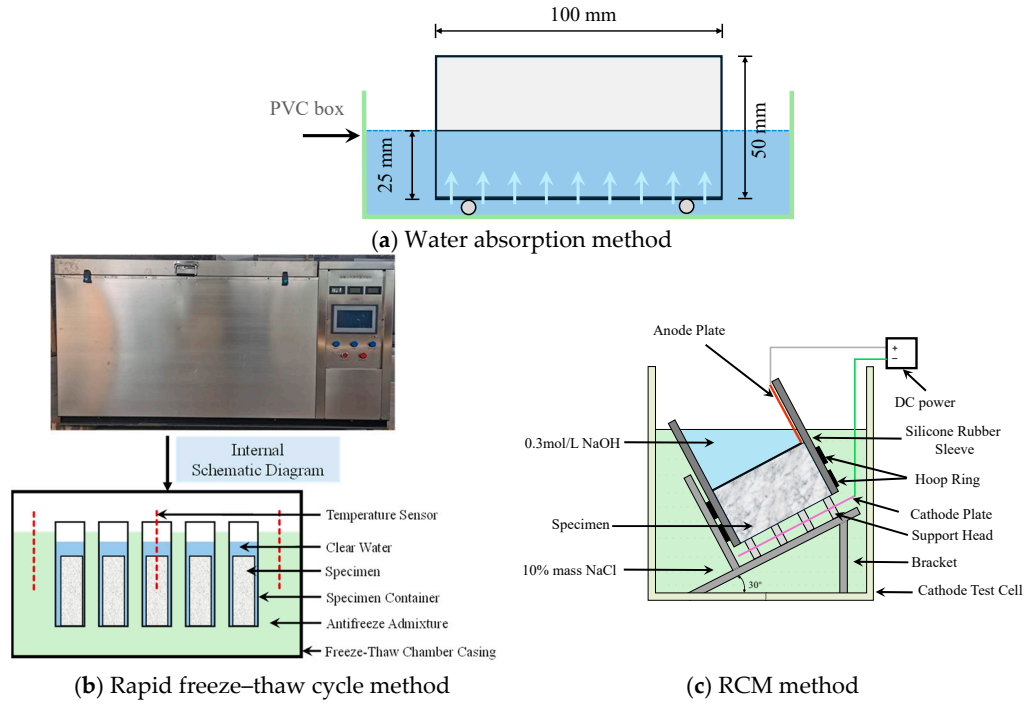
$$W_c^u = \frac{\Omega_u L}{Al} \times 10^3 \quad (2)$$

where, $W_c{}^u$ is the equivalent bending toughness.

The tensile strength test followed the JC/T 2461-2018 "Test methods for mechanical properties of high ductility fiber reinforced cementitious composites" [38]. Standard dog-bone-shaped specimens were used, with a central cross-section of 30 mm × 15 mm and a gauge length of 80 mm. The specimens were subjected to uniaxial tension in an electronic universal testing machine. The loading rate was displacement-controlled at 0.1 mm/min. According to the test procedure, six specimens were used in each group. The average of the six measured values was taken as the initial crack tensile strength, ultimate tensile strength,

and ultimate elongation of the group. The specimen geometry and clamping method are shown in Figure 3d.

For durability performance testing, the tests were conducted in accordance with the GB/T 50081-2019 "Standard for test methods of concrete physical and mechanical properties," the GB/T 50081-2019 "Standard for test methods of concrete physical and mechanical properties," and the GB/T 50082-2024 "Standard for test methods of long-term performance and durability of ordinary concrete" [39], including a water absorption test [40], freeze–thaw cycle, and chloride ion penetration resistance tests. For the water absorption test, the standard 100 mm cubic specimens were used. Each group contained three parallel samples. The specimens were cut to dimensions of 50 mm × 100 mm × 100 mm. Then, they were dried to a constant weight in a forced-air oven at 105 ± 5 °C, with the mass change rate between two consecutive 24 h periods being less than 0.2%. After cooling, the dry mass was accurately measured. The specimens were subsequently fully submerged in a (20 ± 2 °C) constant temperature water bath, with a submersion depth of 25 mm. Following a procedure similar to ASTM C1585 [41], the specimens were removed every 24 h, the surface moisture was carefully wiped off, and the saturated surface-dry mass was recorded [42]. This procedure was repeated until the mass variation between two consecutive measurements was less than 0.2%. The final result was the arithmetic mean of the values from the three specimens. According to the specification, if the maximum or minimum value among the three differs from the median by more than 5%, both the maximum and minimum values are discarded, and the median is taken as the result. If both the maximum and minimum values differ from the median by more than 5%, the test result for that group is considered invalid. The schematic of the test setup is shown in Figure 5a. The rapid freeze–thaw cycle method was used to assess the frost resistance of the concrete. Each condition had three specimens. The specimens were 100 mm × 100 mm × 400 mm prisms, which were cured for 60 days before testing. The freeze–thaw temperature range was set from +20 °C to −20 °C, with each cycle lasting 4 h. The test continued until 200 cycles were completed or the mass loss exceeded 5%. Freeze–thaw cycles were set at 0, 50, 100, 150, and 200 cycles. After the specified number of freeze–thaw cycles, the arithmetic mean of the values of mass loss and dynamic elastic modulus was calculated. A schematic of the test setup is shown in Figure 5b. For chloride ion penetration resistance, the rapid chloride migration (RCM) method was used. The specimens were Φ100 mm × 50 mm cylinders. Each group consisted of three specimens. After saturation, the specimens were placed in the RCM testing device, and a DC voltage was applied at both ends. After the test was completed, the specimen was broken at the center, and a 0.1 mol/L silver nitrate solution was sprayed. The rapid chloride migration coefficient (D_{RCM}) was then calculated according to the measured arithmetic mean of the values for each condition. If the maximum or minimum value deviates from the median by more than 15%, that value is discarded, and the mean of the remaining two values is used. If both the maximum and minimum deviate from the median by more than 15%, the median value is taken as the final result. A schematic of the test setup is shown in Figure 5c.



(**a**) Water absorption method

(**b**) Rapid freeze–thaw cycle method

(**c**) RCM method

Figure 5. Test equipment for the durability tests.

3. Results and Discussion

3.1. Flowability Test Analysis

Figure 6 shows the appearance of HFECC during the flowability test under the four mix ratios. As shown, although there were slight differences in the flow behavior in the details of each mix, the overall flowability performance was relatively similar, with all mixes demonstrating good spreadability. This indicated that all mix ratios exhibited good workability. In HFECC-1, the paste edges were smooth, and the expansion was uniform, suggesting stable flowability. As the BFRP fiber content gradually increased (from 0.20 vol.% to 0.35 vol.%), the change in the expansion range was minimal, and no obvious fiber aggregation or stratification was observed. This indicated that, within the experimental design range, the increase in fiber content did not significantly negatively impact the flowability of the paste. Additionally, the slight adjustment in PE fiber content had a mild effect on flowability, mainly reflected in the uniformity of fiber distribution and the detailed changes in the expansion shape. Overall, all four mixes achieved good fiber dispersion and flow stability, with no segregation or bleeding issues in the paste.

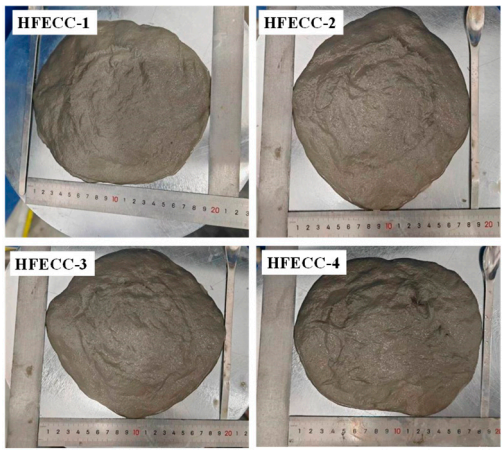


Figure 6. Appearance of the flowability test.

Figure 7 presents the flowability test results of HFECC under the four mix ratios. As shown in the figure, the flowability of the four mixes was approximately 180 mm. As the BFRP fiber content increased from 0.20% vol.% to 0.35% vol.%, while the PE fiber content decreased from 1.40% vol.% to 1.25% vol.%, the flowability initially increased and then decreased. Specifically, when the BFRP content was 0.30% vol.% (HFECC-3), the flowability reached its highest value of 183 mm. However, further increasing the BFRP content to 0.35% vol.% (HFECC-4) caused the flowability to drop to 180 mm, with the expansion decreasing to a minimum value of 176 mm. The observed variation trend was primarily attributed to the combined influence of fiber type, surface characteristics, and volume content. PE fibers were characterized by smooth surfaces and high flexibility [43], which allowed them to be aligned along the flow direction under shear forces, thereby promoting uniform dispersion and reducing flow resistance. In contrast, BFRP fibers were associated with higher stiffness and rough, hydrophilic surfaces, which facilitated water absorption [44] and the formation of a skeletal structure within the cementitious matrix. When the BFRP fiber content was maintained at a moderate level (0.30 vol.%), a slight increase in matrix viscosity was introduced due to the enhanced rigidity, while the reduced PE fiber content led to decreased fiber entanglement, resulting in improved flowability. However, when the BFRP content was further increased to 0.35 vol.%, flowability was reduced, as greater water absorption and intensified fiber interlocking led to higher internal resistance within the matrix. Consequently, the changes in flowability across different mixtures were governed by the synergistic effects of fiber stiffness, fiber–matrix interfacial behavior, and the total fiber volume fraction [45].

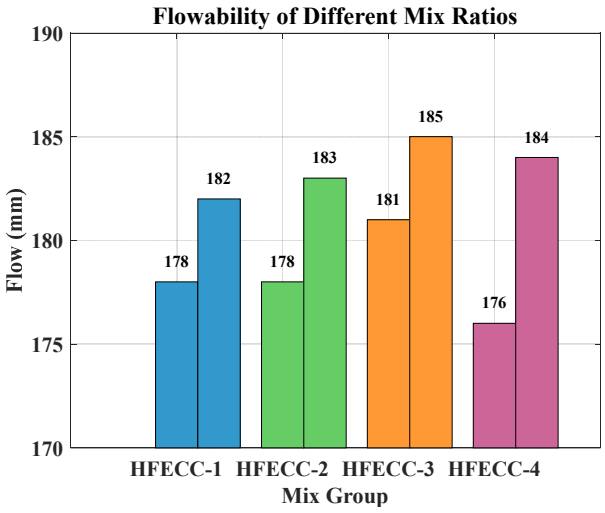


Figure 7. Results of the flowability test.

3.2. Compressive Strength Test Analysis

Figure 8 shows the compressive strength results of HFECC under the four mix ratios. It could be observed that fiber content and mix ratios had a significant impact on the compressive strength. Among them, the HFECC-3 mix exhibited the best compressive performance, with an average compressive strength of 80.71 MPa. This was 16.5%, 11.3%, and 13.0% higher than the values for HFECC-1 (67.41 MPa), HFECC-2 (71.63 MPa), and HFECC-4 (70.2 MPa), respectively. This phenomenon suggested a significant synergistic enhancement effect of the two fibers at a specific ratio. Notably, when the BFRP fiber content exceeded 0.30% vol.% (as in the HFECC-4 mix), the compressive strength significantly dropped. This could be attributed to the excessive BFRP fibers causing a decrease in matrix uniformity, resulting in localized stress concentration points. In addition, longer basalt fibers (15 mm in this study) can form a more effective three-dimensional network within

the concrete matrix, which helps to distribute stress and enhances the overall compressive strength of the structure. This viewpoint was confirmed in the compressive strength tests of BFRP-fiber-reinforced concrete conducted by Zhang et al. [46].

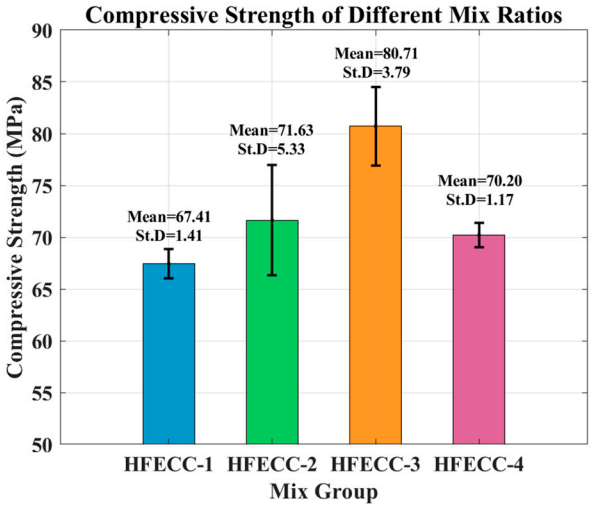


Figure 8. Results of the compressive strength test.

3.3. Three-Point Flexural Strength Test Analysis

Figure 9 presents the results of the three-point flexural strength test of HFECC under the four mix ratios. It could be observed that, as the PE fiber content gradually decreased and the BFRP fiber content gradually increased, the flexural strength of the specimens first increased and then decreased. The highest flexural strength of 26.36 MPa was achieved by the HFECC-3 specimen. Regarding fiber content, in the range from HFECC-1 to HFECC-4, the PE fiber content decreased from 1.40 vol.% to 1.25 vol.%, while the BFRP fiber content increased from 0.20 vol.% to 0.35 vol.%. In the case of HFECC-3, the PE fiber content was 1.30 vol.% and BFRP fiber content was 0.30 vol.%, which resulted in the most significant synergistic effect between the two fibers, showing the best enhancement effect. This was mainly because the PE fibers had excellent ductility and bridging ability, effectively inhibiting the expansion of microcracks and improving material toughness. On the other hand, the BFRP fibers had higher stiffness and strength. These properties could enhance the load-bearing capacity of the components. When the fiber ratio was optimal, the two fibers formed a good synergistic enhancement effect, balancing both toughness and strength and significantly improving the flexural strength. However, when the BFRP fiber content increased further (as in HFECC-4), although the ability to enhance stiffness was improved, the reduction in PE fiber content led to a decrease in toughness. Additionally, there could have been uneven distribution or aggregation of BFRP fibers, resulting in stress concentration and a slight decrease in flexural strength. After the test, the specimens of each group were observed and analyzed based on the failure modes shown in Figure 10. Overall, all of the specimens exhibited typical three-point bending failure. The cracks were mostly located near the center of the loading points, with relatively regular crack propagation paths, and no severe brittle fracture was observed. This indicated that the incorporation of fibers had a good inhibitory effect on crack propagation. Specifically, the HFECC-1 and HFECC-2 groups had larger crack widths due to the lower BFRP fiber content, suggesting that their load-bearing and crack resistance performance had not reached the optimal state. The HFECC-3 group not only showed the highest flexural strength, but also exhibited finer and more evenly distributed cracks with a more ductile failure mode, demonstrating good energy dissipation ability. The HFECC-4 group, although having a higher BFRP fiber

content, showed more localized cracks and some brittle behavior, possibly due to fiber aggregation, leading to uneven distribution [45].

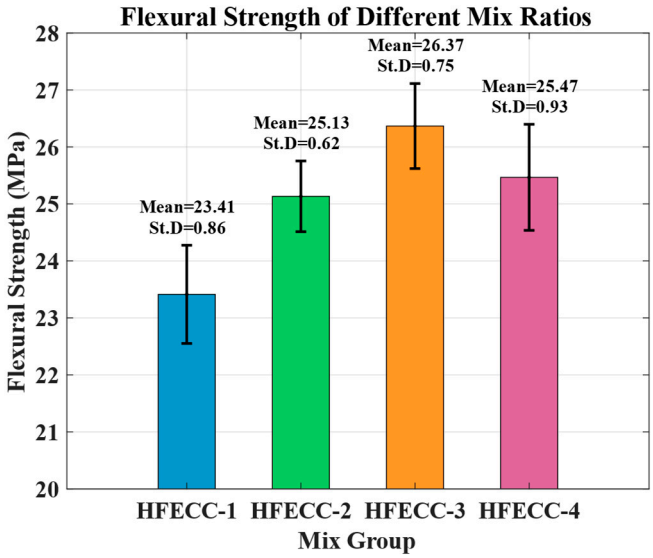


Figure 9. Results of the three-point flexural strength test.

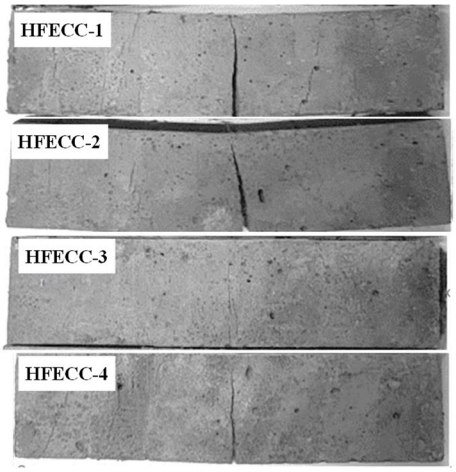
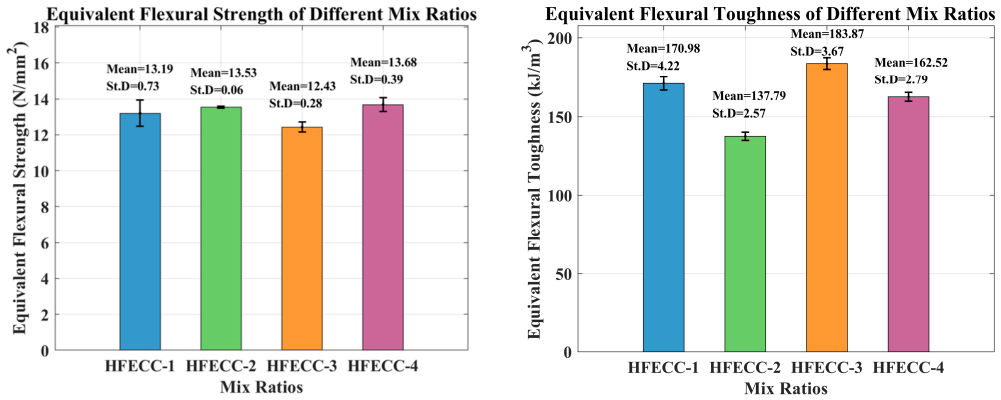


Figure 10. The failure modes of specimens.

3.4. Four-Point Equivalent Bending Strength and Toughness Test Analysis

The equivalent bending strength and toughness of specimens with different fiber composite ratios are shown in Figure 11. In terms of equivalent bending strength, the values of the four groups fluctuated slightly, with the average ranging from 12.43 to 13.68 N/mm^2. The HFECC-4 group exhibited the highest equivalent bending strength (13.68 N/mm^2), followed by HFECC-2 (13.53 N/mm^2), and the lowest was HFECC-3 (12.43 N/mm^2). This suggests that, with the increase in BFRP fiber content, its higher modulus and rigidity enhanced the initial load-bearing capacity of the specimens to a certain extent. Particularly in HFECC-4, with a BFRP fiber content of 0.35 vol.%, the enhancement effect was more pronounced. In contrast, the PE fibers mainly contributed to ductility, with a weaker direct enhancement effect on strength. Therefore, although HFECC-3 had a higher PE fiber content, its equivalent bending strength was slightly lower. However, the results of equivalent bending toughness showed significant differences between the different ratios. The equivalent bending toughness of HFECC-3 reached 183.87 kJ/m^3, the highest among the four groups, approximately 33.4% higher than that of HFECC-2 (137.79 kJ/m^3), indicating better energy absorption ability and fracture ductility. The equivalent bending

toughness of HFECC-1 and HFECC-4 was at an intermediate level, at 170.98 kJ/m^3 and 162.52 kJ/m^3, respectively. Based on the ratio analysis, in HFECC-3, the PE and BFRP fiber contents were 1.30 vol.% and 0.30 vol.%, respectively. This combination optimally balanced crack control and fiber bridging and energy dissipation mechanisms, significantly improving the material's equivalent bending toughness.



(**a**) Four-point equivalent bending strength (**b**) Four-point equivalent bending toughness

Figure 11. Four-point equivalent bending strength and toughness test results.

Figure 12 presents the typical bending failure morphology of the four groups of specimens. It can be observed that the specimens of HFECC-1, HFECC-2, and HFECC-4 developed primary cracks earlier under load, exhibiting a certain degree of brittle failure. In contrast, the HFECC-3 specimens showed a more uniform crack distribution and greater deformation capacity during bending failure, with multiple small cracks forming, indicating ductile behavior [37]. This phenomenon further verified the consistency between the equivalent bending toughness results and the failure morphology.

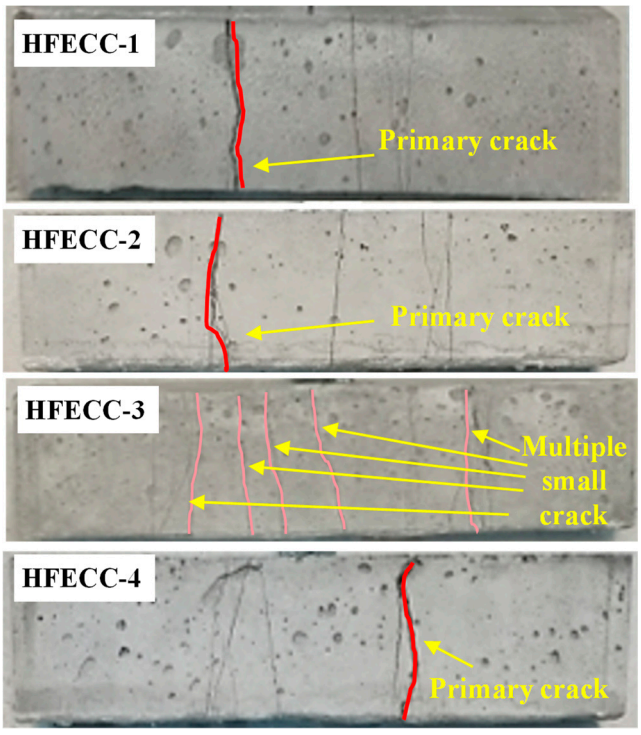
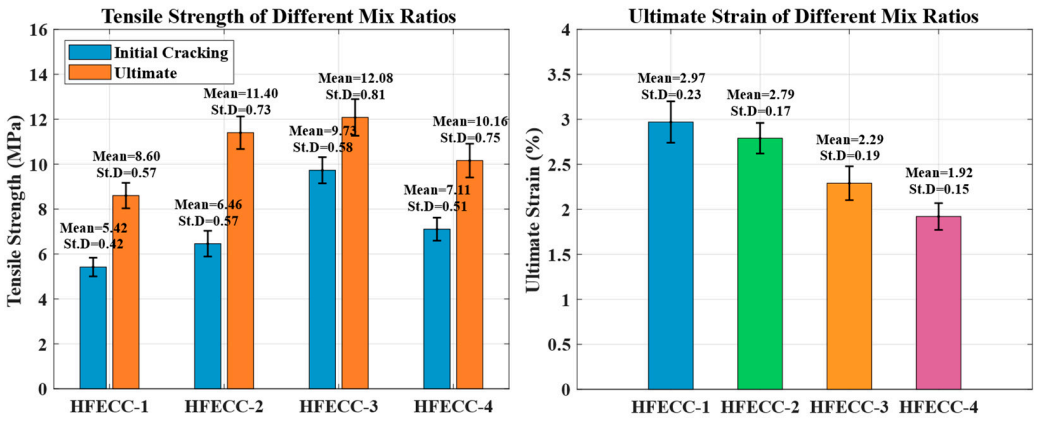


Figure 12. Four-point bending specimen failure morphology.

3.5. Tensile Strength Test Analysis

Figure 13 shows the initial crack tensile strength, ultimate tensile strength, and ultimate elongation of the specimens with different mix ratios. In terms of initial crack tensile strength, with the increase in BFRP fiber content in the mix ratio, the initial crack strength showed an increasing trend. Specifically, HFECC-3 reached the highest value of 9.728 MPa, significantly higher than the other groups. HFECC-2 and HFECC-4 had values of 6.46 MPa and 7.11 MPa, respectively, while HFECC-1 had the lowest at 5.42 MPa. This suggests that the inclusion of BFRP fibers effectively improved the material's crack resistance. The high elastic modulus and strong interfacial bonding properties of BFRP fibers helped suppress cracks before microcracks formed, thereby increasing the initial crack stress level. Regarding ultimate tensile strength, HFECC-3 was still the highest among the four groups, reaching 12.08 MPa. HFECC-2 followed at 11.4 MPa, while HFECC-1 and HFECC-4 had values of 8.6 MPa and 10.16 MPa, respectively. This trend indicates that BFRP fibers are effective in enhancing post-crack load-bearing capacity, particularly in HFECC-3, where the BFRP fibers (0.30 vol.%) and PE fibers (1.30 vol.%) form an optimal synergy, ensuring sustained tensile force in the post-crack phase and delaying the final failure of the material. This trend was similar to the findings of Dias and Thaumaturgo [23]. According to their research, BFRP-fiber-reinforced cement-based materials primarily experience fiber pull-out failure under tension, and the fiber pull-out improves the material's performance after cracking. Branston et al. [24] also found that basalt-fiber-reinforced concrete improved pre-crack strength, and the fiber pull-out mechanism further enhanced post-crack performance.



(**a**) Tensile strength (**b**) Ultimate elongation

Figure 13. Tensile strength test results.

However, in terms of ultimate elongation, the data exhibited an opposite trend to that of strength-related parameters. The elongation of HFECC-1 was the highest at 2.97%, followed by HFECC-2 at 2.79%, HFECC-3 at 2.29%, and HFECC-4 at the lowest, with only 1.92%. This indicates that, as the BFRP fiber content increased, the material's overall ductility gradually decreased. The reason for this is that BFRP fibers, with higher rigidity and brittleness, can improve load-bearing capacity but have poor adaptability to crack propagation, which limits the elongation capability of the specimens during the tensile phase. Although PE fibers have good toughness and tensile ability, their main function is to improve the material's strain capacity and post-crack ductility. As the PE fiber content gradually decreased (e.g., in HFECC-4, it was only 1.25 vol.%), its crack-bridging and energy dissipation abilities diminished, leading to a significant reduction in elongation.

3.6. Water Absorption Test Analysis

Figure 14 presents the water absorption results of the four groups of HFECC specimens. The absorption values are relatively close, measured at 0.430% (HFECC-3), 0.433% (HFECC-1), and 0.437% (HFECC-2 and HFECC-4), with standard deviations ranging from 0.015% to 0.025%. This indicates good consistency and stability in the water absorption performance across different HFECC mix designs, with minimal variability among specimens. The similarity in water absorption can be attributed to the comparable pore structure characteristics of the specimens. All HFECC mixtures incorporated a certain volume fraction of basalt-fiber-reinforced polymer (BFRP), which plays a bridging and filling role during the hardening process [47]. This helps to control microcrack propagation and reduce pore connectivity, thereby limiting water migration paths. Moreover, all groups included a relatively high dosage of mineral admixtures (such as fly ash), which contributed to the formation of additional calcium silicate hydrate (C–S–H) gel through continued hydration, enhancing matrix densification [48]. Therefore, despite slight variations in fiber content or matrix composition, their influence on water absorption was minimal, and the overall resistance to water ingress remained consistently high across all groups.

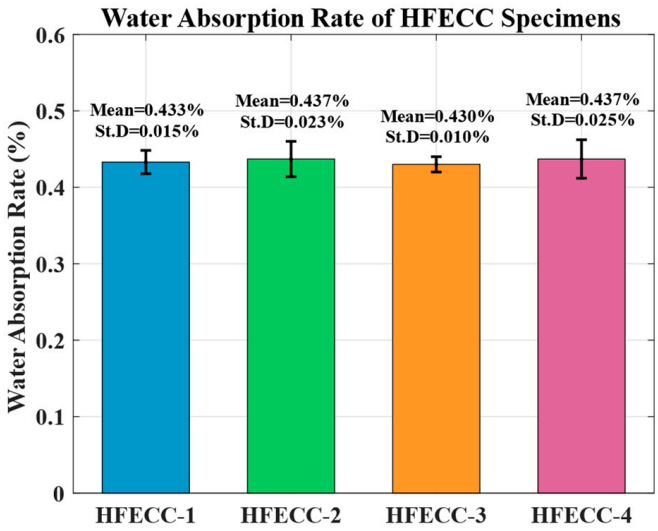
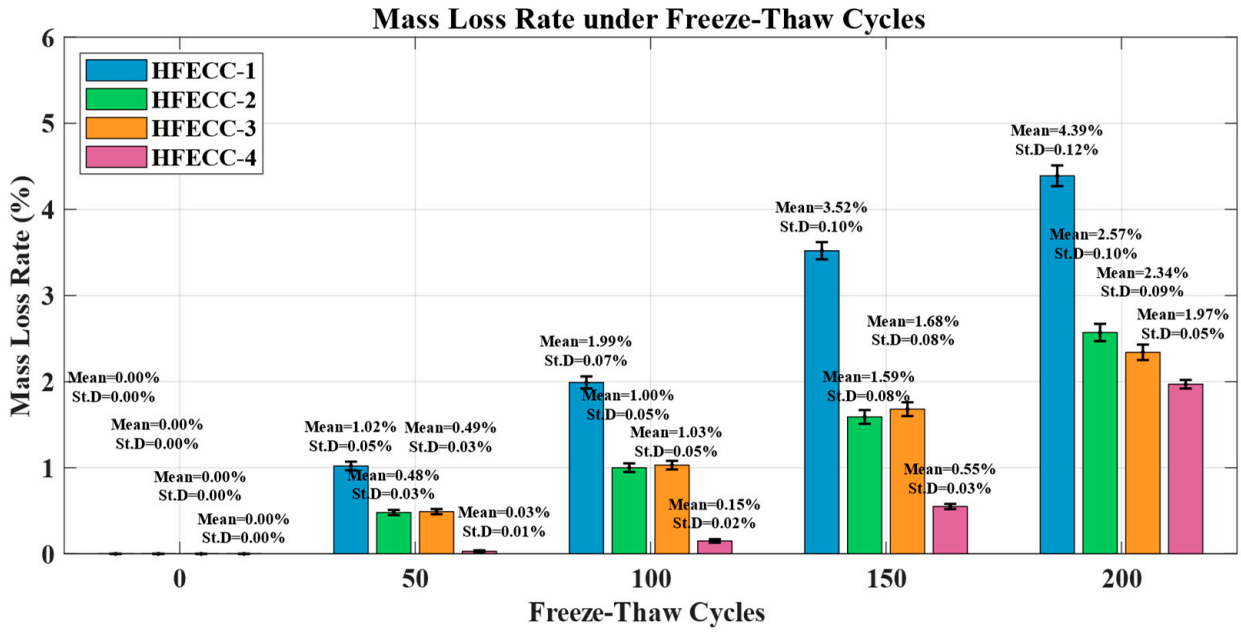


Figure 14. Water absorption test results.

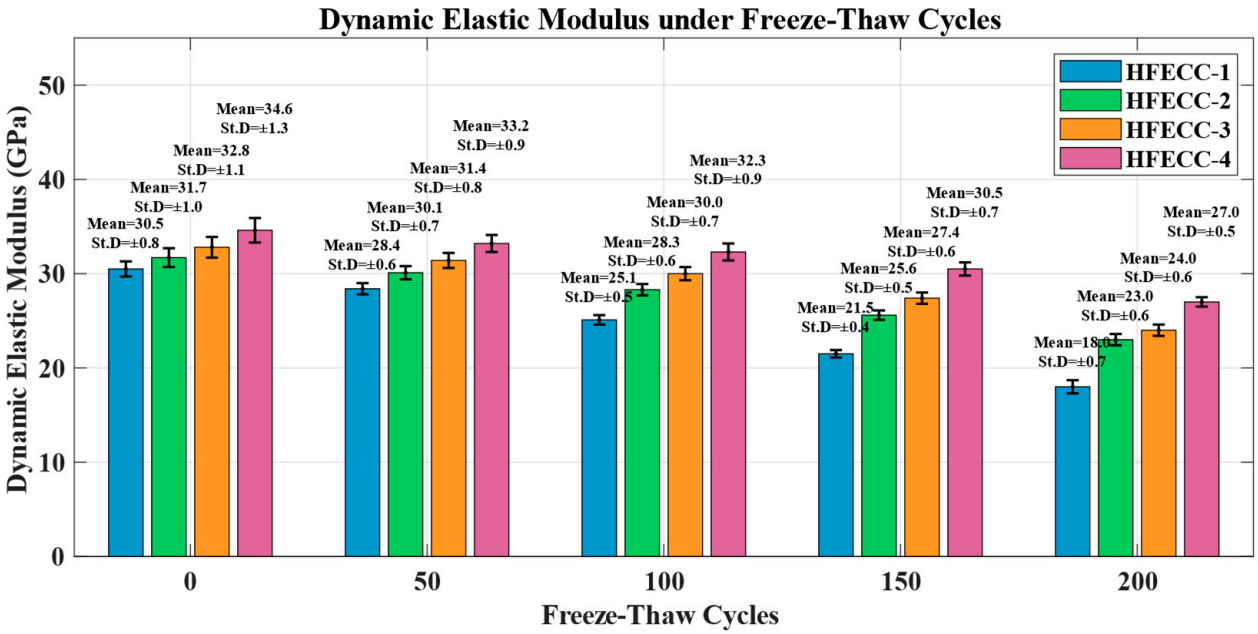
3.7. Freeze–Thaw Cycle Test Analysis

Figure 15a shows the mass loss rate of specimens under different mix ratios with the increase in freeze–thaw cycles. It can be seen that, from 0 to 200 freeze–thaw cycles, the mass of all groups decreased to different extents, and the mass loss rate increased as the number of freeze–thaw cycles progressed. After 50 freeze–thaw cycles, the mass loss rate of HFECC-1 was 1.02%, significantly higher than that of HFECC-2 (0.48%), HFECC-3 (0.49%), and HFECC-4 (0.03%). As the number of freeze–thaw cycles increased to 100, 150, and 200, this trend remained evident. After 200 freeze–thaw cycles, the mass loss rate of HFECC-1 increased to 4.39%, nearly 2.2 times that of HFECC-4 (1.97%), indicating the poorest freeze–thaw performance. On the other hand, HFECC-4 consistently exhibited the lowest mass loss rate, with the most gradual increase throughout the entire freeze–thaw process, demonstrating the best freeze–thaw durability. Further observation of the freeze–thaw stability of the four groups revealed that the mass loss rates of HFECC-2 and HFECC-3 were very close throughout the entire testing period. The maximum difference did not exceed 0.23%. This indicates that both mixes, with BFRP fiber contents of 0.25 vol.% and 0.30 vol.%, respectively, exhibited good freeze–thaw resistance. In contrast, the BFRP fiber content in HFECC-1 was only 0.20 vol.%, and its freeze–thaw resistance was significantly

reduced, while HFECC-4, with a BFRP fiber content of 0.35 vol.%, demonstrated the best performance among all mixes. It should be noted that HFECC-4 had the lowest ultimate elongation (1.92%) among the four groups, which may limit its application in structures requiring high ductility. In contrast, HFECC-3 achieved a more favorable balance between ductility and environmental resistance. With an ultimate elongation of 2.29% and a mass loss rate of only 2.08% after 200 freeze–thaw cycles, HFECC-3 demonstrated both satisfactory freeze–thaw durability and relatively high deformation capacity. This suggests that HFECC-3 offers a well-balanced fiber hybridization strategy, making it more suitable for structural applications where both mechanical flexibility and environmental durability are critical.



(**a**) Mass loss rate



(**b**) Dynamic elastic modulus

Figure 15. The freeze–thaw cycle test results.

The dynamic elastic modulus results of the four HFECC specimens are shown in Figure 15b. The initial dynamic elastic modulus of all four materials ranged from 30 to 35 GPa, with an overall increasing trend as the BFRP fiber content increased. The initial dynamic elastic modulus of HFECC-1 was 30.5 GPa. This was the lowest among the four groups. HFECC-4's initial modulus reached 34.6 GPa, an increase of approximately 13.4%. This indicates that higher BFRP fiber content helps to improve the overall stiffness of the material. It also enhances its ability to resist elastic deformation. Additionally, as the number of freeze–thaw cycles increased, the dynamic elastic modulus of all four HFECC specimens gradually decreased. HFECC-1 experienced the most significant modulus reduction. It dropped from 30.5 GPa to 18.0 GPa, a decrease of about 41.0%. This reduction corresponded to its highest mass loss rate, which was 4.39%. The performance degradation of HFECC-2 and HFECC-3 was moderate. Their dynamic elastic moduli decreased to 23.0 GPa and 24.0 GPa after 200 freeze–thaw cycles, respectivley. This indicates a certain freeze–thaw stability. HFECC-4 exhibited the best freeze–thaw performance. Its modulus decreased from 34.6 GPa to 27.0 GPa, a reduction of only 22.0%. This trend aligns with its lowest mass loss rate, which was 1.97%. This suggests that a higher BFRP fiber content plays a significant role in enhancing the material's freeze–thaw resistance and maintaining structural integrity. The experimental results from the freeze–thaw tests show that an increase in BFRP fiber content significantly enhances the freeze–thaw resistance of HFECC materials. BFRP fibers play a key role in preventing the development of microcracks during freeze–thaw cycles, thus minimizing the damage caused by the migration and expansion of moisture and ice crystals within the material. Furthermore, the high PE fiber content contributes to improving the material's toughness and delaying crack propagation. This combination of effects leads to a synergistic improvement in overall performance. A similar phenomenon was also observed by Wang et al. in their study on the frost resistance of cement-based composites with added BFRP fibers [27].

3.8. Chloride Ion Penetration Resistance Test Analysis

The chloride ion migration coefficients D_{RCM} of the four groups of HFECC specimens are shown in Figure 16. The results indicate that the migration coefficients of all specimens fall within the RCM-IV grade range, demonstrating good resistance to chloride ion penetration. Overall, as the BFRP fiber content increases, the chloride ion migration coefficient gradually decreases, indicating an improvement in impermeability. Among the specimens, the migration coefficient of HFECC-1 was 10.2×10^{-13} m^2/s, the highest among the four groups. In contrast, HFECC-4 had the lowest migration coefficient of 6.3×10^{-13} m^2/s, showing the best resistance to chloride ion penetration. This trend suggests that the incorporation of BFRP fibers significantly improves the density of the cement-based composites. BFRP fibers effectively block the migration path of chloride ions and reduce their diffusion rate. According to the studies conducted by Liu [29], BFRP fibers could create a three-dimensional network structure through physical obstruction, significantly increasing the tortuosity of chloride ion migration paths and reducing their diffusion rate by elongating the transport trajectory. As demonstrated by Wang et al. [28], the BFRP fibers could effectively inhibit microcrack propagation, thereby minimizing interconnected permeation channels. This mechanism restricts chloride penetration depth. These findings indicate that a suitable amount of BFRP fibers can effectively enhance the microstructure of cement-based composites, improving their resistance to chloride ion penetration and thus increasing the material's service durability in chloride-containing environments. The excellent performance of HFECC-4 further validates the potential application of BFRP fibers in enhancing material durability.

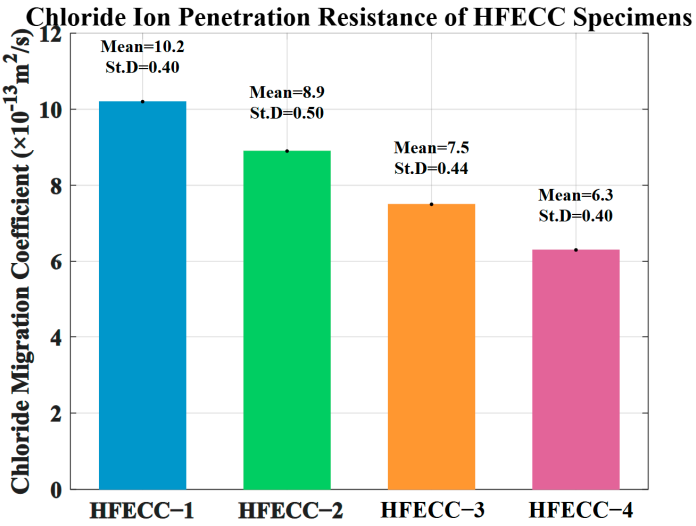


Figure 16. The chloride ion migration coefficients D_{RCM}.

3.9. SEM Result and Analysis

To further investigate the synergistic toughening mechanism of PE fibers and BFRP fibers in the HFECC-3 composite, SEM observations [49,50] were conducted on the fracture surfaces of specimens after the four-point bending test, as shown in Figure 17. Figure 17a shows that the BFRP fibers are evenly distributed in the cement matrix, with strong interface bonding. The good dispersion of BFRP fibers is attributed to their inorganic nature and density, which are similar to those of the cement matrix, thus helping to prevent interface delamination during the molding process and enhancing the bonding strength and collaborative load-bearing capacity in the interface region. Figure 17b displays the surface microstructure of the PE fibers under load. Compared to BFRP fibers, the surface of PE fibers is rougher, with more micropores in the interface transition zone, and their cross-section presents an irregular shape, exhibiting typical plastic deformation characteristics. This phenomenon indicates that the PE fibers undergo significant slip and frictional energy dissipation during loading, with surface twisting and scratches revealing their important role in stress transfer and crack propagation control, effectively improving the overall toughness of the material [13]. Figure 17c shows the fracture morphology of the BFRP fibers. Compared to Figure 17b, the difference in failure modes between the two types of fibers is more apparent. BFRP fibers primarily exhibit brittle fracture, with smooth fracture surfaces, indicating rapid failure after reaching ultimate strength. In contrast, PE fibers predominantly fail by pull-out, with distinct shear marks and plastic deformation traces on the fiber surface, leaving pull-out marks in the matrix. This difference in failure behavior demonstrates that the PE fibers can continuously dissipate energy through the pull-out process during the crack propagation stage, enhancing the material's ductile response. Figure 17d reveals the synergistic toughening mechanism of the composite fibers. Due to the strong hydrophobicity of the PE fibers, the interface bond strength with the matrix is relatively weak, which leads to pull-out behavior during loading. This provides a certain degree of ductile buffering effect during the initial crack initiation and propagation stages. On the other hand, BFRP fibers can maintain an effective bridging state at higher stress levels, delaying further crack propagation. The two fibers work synergistically at different stress stages, forming a multi-stage energy dissipation mechanism that gradually interrupts crack propagation, effectively improving the mechanical strength and toughness of the material.

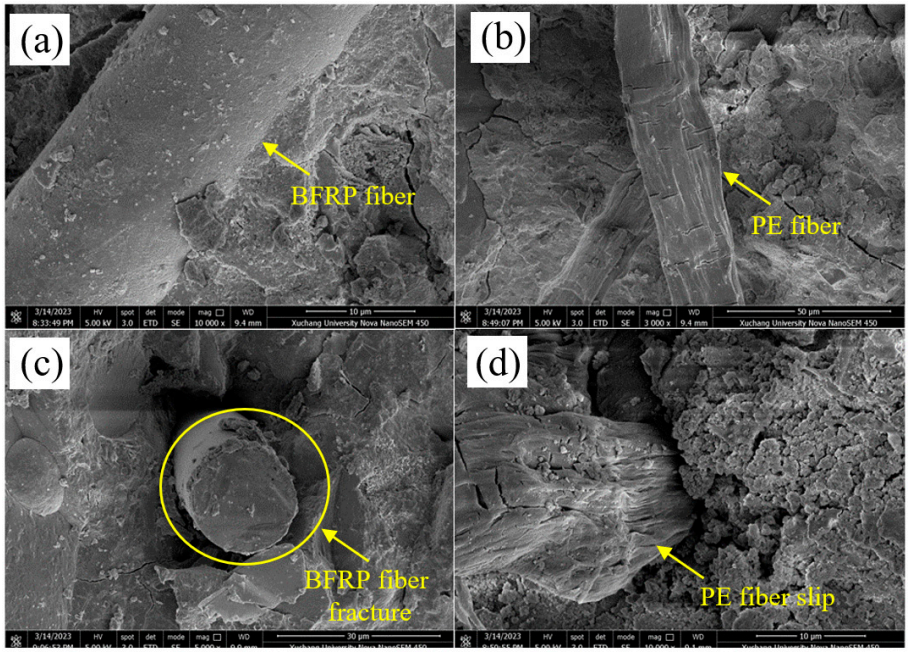


Figure 17. SEM images: (**a**) morphology of BFRP fibers; (**b**) morphology of PE fibers; (**c**) fracture failure of BFRP fibers; (**d**) slip failure of PE fibers.

4. Conclusions

This study systematically investigates the preparation and performance analysis of a PE-BFRP hybrid-fiber-engineered cementitious composite. By controlling the volume fraction ratio of PE fibers to BFRP fibers, multiple sets of HFECC specimens were prepared. Theoretical research was conducted through flowability tests, mechanical property tests, and durability tests. The main conclusions of this study are as follows:

(1) HFECC with a total fiber volume of 1.6% (PE + BFRP) shows good workability, with flowability of around 180 mm for all mix ratios.

(2) As the BFRP content increases, compressive, flexural, and tensile strengths first rise and then decline. HFECC-3 (0.30% BFRP + 1.30% PE) achieves the best overall mechanical performance. While fiber ratio changes have little impact on equivalent bending strength, HFECC-3 exhibits the highest bending toughness. However, elongation decreases with more BFRP fibers due to their higher stiffness and brittleness.

(3) Freeze–thaw resistance improves with increased BFRP content. When BFRP increases from 0.20% to 0.35%, the mass loss rate after 200 cycles drops from 4.39% to 1.97%. Simultaneously, the initial dynamic elastic modulus increases from 30.5 GPa to 34.6 GPa. After freeze–thaw cycles, the modulus of the 0.35% BFRP mix remains higher (27.0 GPa) than that of the 0.20% mix (18.0 GPa), indicating improved durability. With increasing BFRP content, chloride ion penetration resistance is enhanced due to the formation of a three-dimensional fiber network that physically obstructs ion transport and mitigates microcrack propagation. The migration coefficient decreases from 10.2×10^{-13} m^2/s to 6.3×10^{-13} m^2/s when the BFRP volume increases from 0.20% to 0.35%.

(4) SEM analysis shows a synergistic effect between PE and BFRP fibers. The combined bridging and pull-out mechanisms enhance both strength and toughness. These findings suggest that hybrid fiber reinforcement effectively balances strength, ductility, and durability in HFECC.

Author Contributions: Conceptualization, S.X.; Methodology, S.X.; Software, W.L.; Validation, W.L.; Formal analysis, W.L. and H.J.; Investigation, X.W. (Xuezhen Wang); Data curation, X.W. (Xuezhen Wang), H.Z., J.L., X.W. (Xuebin Wang), H.M., J.S. and Z.Y.; Writing—original draft, S.X. and K.D.; Writing—review and editing, K.D.; Visualization, K.D. All authors have read and agreed to the published version of the manuscript.

Funding: The research in this paper has received financial support from the Natural Science Foundation of China (project number: 52408564), the China Postdoctoral Science Foundation (project number: 2023M733247), the Joint Fund for Science and Technology Research and Development Program of Henan Province (project number: 242301420027), and the central finance of Guangxi Zhuang Autonomous Region Guides Local Science and Technology Development Funds (project number: 2023ZYZX1003).

Data Availability Statement: The original contributions presented in the study are included in the article; further inquiries can be directed to the corresponding author.

Conflicts of Interest: Author Shasha Xu, Wei Li, Xuezhen Wang, Hongze Zhang, Ju Liu, Hui Jiang, Xuebin Wang were employed by the SINO-SINA Building Materials Co., Ltd. The remaining authors declare that the research was conducted in the absence of any commercial or financial relationships that could be construed as a potential conflict of interest.

References

1. Li, V.C.; Leung, C.K.Y. Steady-State and Multiple Cracking of Short Random Fiber Composites. *J. Eng. Mech.* **1992**, *118*, 2246–2264. [CrossRef]
2. Li, V. From Micromechanics to Structural Engineering—The Design of Cementitous Composites for Civil Engineering Applications. *Struct. Eng. Earthq. Eng.* **1994**, *10*, 1–34.
3. Ma, H.; Zhang, Z. Paving an engineered cementitious composite (ECC) overlay on concrete airfield pavement for reflective cracking resistance. *Constr. Build. Mater.* **2020**, *252*, 119048. [CrossRef]
4. Shoji, D.; He, Z.; Zhang, D.; Li, V.C. The greening of engineered cementitious composites (ECC): A review. *Constr. Build. Mater.* **2022**, *327*, 126701. [CrossRef]
5. Liu, Y.; Wu, W.-Z.; Zhang, Y.-X.; Hou, W.; Zhang, H.; Peng, L.-G. Engineered/strain-hardening cementitious composites (ECC/SHCC) for resilient cold-region infrastructure: A critical review of freeze-thaw durability. *Case Stud. Constr. Mater.* **2025**, *22*, e04362. [CrossRef]
6. Wu, W.-Z.; Zhang, Y.-X.; Liu, Y.; Hou, W.; Zhu, J.-X.; Jiang, F.; Xu, L.-Y. Impacts of chloride salt, freeze-thaw cycling, and pre-cracking on mechanical properties of Engineered Cementitious Composites (ECC). *Constr. Build. Mater.* **2025**, *475*, 141221. [CrossRef]
7. Khan, M.; Ali, M. Use of glass and nylon fibers in concrete for controlling early age micro cracking in bridge decks. *Constr. Build. Mater.* **2016**, *125*, 800–808. [CrossRef]
8. Zhao, C.; Wang, Z.; Zhu, Z.; Guo, Q.; Wu, X.; Zhao, R. Research on different types of fiber reinforced concrete in recent years: An overview. *Constr. Build. Mater.* **2023**, *365*, 130075. [CrossRef]
9. Loukil, M.; Hassine, W.B.; Limam, O.; Kotronis, P. Experimental determination of GFRC tensile parameters from three-point bending tests using an analytical damage model. *Constr. Build. Mater.* **2019**, *223*, 477–490. [CrossRef]
10. Wang, W.; Li, L.; Chen, J.; Dai, K. Experimental and analytical study on flexural behavior of corroded RC beams strengthened with CFRP rods and UHPC. *Eng. Struct.* **2025**, *323*, 119299. [CrossRef]
11. Pan, Z.; Wu, C.; Liu, J.; Wang, W.; Liu, J. Study on mechanical properties of cost-effective polyvinyl alcohol engineered cementitious composites (PVA-ECC). *Constr. Build. Mater.* **2015**, *78*, 397–404. [CrossRef]
12. Li, V.; Wu, C.; Wang, S.X.; Ogawa, A.; Saito, T. Interface tailoring for strain-hardening polyvinyl alcohol-engineered cementitious composite (PVA-ECC). *ACI Mater. J.* **2002**, *99*, 463–472.
13. Liu, D.; Yu, J.; Qin, F.; Zhang, K.; Zhang, Z. Mechanical performance of high-strength engineering cementitious composites (ECC) with hybriding PE and steel fibers. *Case Stud. Constr. Mater.* **2023**, *18*, e01961. [CrossRef]
14. Huo, Y.; Liu, T.; Lu, D.; Han, X.; Sun, H.; Huang, J.; Ye, X.; Zhang, C.; Chen, Z.; Yang, Y. Dynamic tensile properties of steel fiber reinforced polyethylene fiber-engineered/strain-hardening cementitious composites (PE-ECC/SHCC) at high strain rate. *Cem. Concr. Compos.* **2023**, *143*, 105234. [CrossRef]
15. Yu, K.; Ding, Y.; Liu, J.; Bai, Y. Energy dissipation characteristics of all-grade polyethylene fiber-reinforced engineered cementitious composites (PE-ECC). *Cem. Concr. Compos.* **2020**, *106*, 103459. [CrossRef]

16. Liu, L.; Xiao, J.; Wu, Z. The effect of fiber content on the static and dynamic performance of PE-ECC. *Case Stud. Constr. Mater.* **2024**, *20*, e03041. [CrossRef]
17. Wang, Z.; Liang, X.; Zhai, T. Predicting the flexural behavior of steel-PVA hybrid fiber reinforced cementitious composite. *Structures* **2023**, *51*, 1189–1204. [CrossRef]
18. Hou, M.; Li, V.C. Tailoring crack width control of LC3-based engineered cementitious composites (ECC) via fiber hybridization: From micromechanics design to macro investigation. *Mater. Des.* **2023**, *235*, 112433. [CrossRef]
19. Ahmed, S.F.U.; Maalej, M.; Paramasivam, P. Flexural responses of hybrid steel–polyethylene fiber reinforced cement composites containing high volume fly ash. *Constr. Build. Mater.* **2007**, *21*, 1088–1097. [CrossRef]
20. Zhou, Y.; Xi, B.; Yu, K.; Sui, L.; Xing, F. Mechanical Properties of Hybrid Ultra-High Performance Engineered Cementitous Composites Incorporating Steel and Polyethylene Fibers. *Materials* **2018**, *11*, 1448. [CrossRef]
21. Tinoco, M.P.; de Andrade Silva, F. On the mechanical behavior of hybrid fiber reinforced strain hardening cementitious composites subjected to monotonic and cyclic loading. *J. Mater. Res. Technol.* **2021**, *11*, 754–768. [CrossRef]
22. Özkan, Ş.; Demir, F. The hybrid effects of PVA fiber and basalt fiber on mechanical performance of cost effective hybrid cementitious composites. *Constr. Build. Mater.* **2020**, *263*, 120564. [CrossRef]
23. Dias, D.P.; Thaumaturgo, C. Fracture Toughness of Geopolymeric Concretes Reinforced with Basalt Fibers. *Cem. Concr. Compos.* **2005**, *27*, 74–75. [CrossRef]
24. Branston, J.; Das, S.; Kenno, S.Y.; Taylor, C. Mechanical Behavior of Basalt Fiber Reinforced Concrete. *Constr. Build. Mater.* **2016**, *124*, 878–886. [CrossRef]
25. Ayub, T.; Shafiq, N.; Nuruddin, M.F. Mechanical Properties of High-Performance Concrete Reinforced with Basalt Fibers. *Procedia Eng.* **2014**, *77*, 131–139. [CrossRef]
26. Zhou, H.; Jia, B.; Huang, H.; Mou, Y. Experimental Study on Basic Mechanical Properties of Basalt Fiber Reinforced Concrete. *Materials* **2020**, *13*, 1362. [CrossRef]
27. Wang, Z.T. Experimental Study on the Frost Resistance of Basalt Fiber Reinforced Concrete. Master's Thesis, Harbin Engineering University, Harbin, China, 2017. (In Chinese)
28. Wang, Z.S.; Xing, L.X.; Wu, B.; Zhang, Y. Study on the Effect of Basalt Fiber Content on the Durability of Concrete Under Sulfate Corrosion. *Build. Struct.* **2020**, *50*, 91–95+46. (In Chinese)
29. Liu, Y. Experimental Study and Mechanism Analysis of Basalt Fiber Reinforced Concrete in Acidic Environment. Master's Thesis, Xi'an University of Technology, Xi'an, China, 2017. (In Chinese)
30. *GB 175-2007*; Common Portland Cement. Standardization Administration of China: Beijing, China, 2007.
31. *ASTM C150/C150M-22*; Standard Specification for Portland Cement. ASTM International: West Conshohocken, PA, USA, 2022.
32. *EN 197-1:2011*; Cement—Part 1: Composition, Specifications and Conformity Criteria for Common Cements. European Committee for Standardization (CEN): Brussels, Belgium, 2011.
33. *GB/T 2419-2005*; Test Method for Fluidity of Cement Mortar. Standardization Administration of China: Beijing, China, 2005. (In Chinese)
34. *GB/T 50081-2019*; Standard for Test Method of Mechanical Properties on Ordinary Concrete. Ministry of Housing and Urban-Rural Development of the People's Republic of China: Beijing, China, 2019. (In Chinese)
35. *GB/T 17671-2021*; Test Method of Mechanical Properties of Cement Mortar. Standardization Administration of China: Beijing, China, 2021. (In Chinese)
36. *DBJ41/T 236-2020*; Technical Specification for Application of Recycled Concrete in Buildings. Department of Housing and Urban-Rural Development of Henan Province: Zhengzhou, China, 2020. (In Chinese)
37. Zhang, Y.; Zhang, S.; Deng, M. Four-point bending tests of ECC: Mechanical response and toughness evaluation. *Case Stud. Constr. Mater.* **2022**, *17*, e01573. [CrossRef]
38. *JC/T 2461-2018*; Technical Specification for Recycled Fine Aggregate for Concrete and Mortar. Ministry of Industry and Information Technology of the People's Republic of China: Beijing, China, 2018. (In Chinese)
39. *GB/T 50082-2024*; Standard for Durability Test Method of Ordinary Concrete. Ministry of Housing and Urban-Rural Development of the People's Republic of China: Beijing, China, 2024. (In Chinese)
40. Sabir, B.B.; Wild, S.; O'Farrell, M. A water sorptivity test for mortar and concrete. *Mater. Struct.* **1998**, *31*, 568–574. [CrossRef]
41. *ASTM C1585-20*; Standard Test Method for Measurement of Rate of Absorption of Water by Hydraulic-Cement Concretes. ASTM International: West Conshohocken, PA, USA, 2020.
42. Kabir, H.; Wu, J.; Dahal, S.; Joo, T.; Garg, N. Automated Estimation of Cementitious Sorptivity via Computer Vision. *Nat. Commun.* **2024**, *15*, 53993. [CrossRef]
43. Niu, R.; Yang, Y.; Liu, Z.; Ding, Z.; Peng, H.; Fan, Y. Durability of Two Epoxy Adhesive BFRP Joints Dipped in Seawater under High Temperature Environment. *Polymers* **2023**, *15*, 3232. [CrossRef] [PubMed]
44. Wawkuschewski, A.; Cantow, H.J.; Magonov, S.N. Surface morphology and nanostructure of high modulus polyethylene fiber. *Polym. Bull.* **1994**, *32*, 235–240. [CrossRef]

45. Zhang, Z.; Ji, Y.; Ji, W. Durability Performance Investigation for Engineering Fiber Cementitious Composites (ECC): Review. *Polymers* **2023**, *15*, 931. [CrossRef] [PubMed]
46. Zhang, Y.; Wang, L.; Li, H.; Liu, Y.; Zhao, X.; Zhang, T. Compressive Properties of Basalt Fibers and Polypropylene Fiber-Reinforced Lightweight Concrete. *ACS Omega* **2023**, *9*, 26973–26982. [CrossRef]
47. Jia, T.F.; Liu, H.W.; Chu, F.J.; Sun, H.; Yang, S.W.; Yang, T.Y. Water Absorption of Basalt Fiber Reinforced Cement. *Adv. Mater. Res.* **2012**, *627*, 823–826. [CrossRef]
48. Wang, S.; Liu, J.; Tian, Y.; Zhao, P. Influence of Composite C-S-H Seed Prepared by Wet Grinding on High-Volume Fly Ash Concrete. *Buildings* **2025**, *15*, 270. [CrossRef]
49. Dai, K.; Li, S.; Hu, P.; Jiang, N.; Wang, D. Effect of outer rust layer on cathodic protection and corrosion behavior of high-strength wire hangers with sheath crack in marine rainfall environment. *Case Stud. Constr. Mater.* **2023**, *18*, e02043. [CrossRef]
50. Hu, P.; Li, S.; Dai, K.; Jiang, N.; Wang, D. Analysis of hydrogen embrittlement and applied potential of 1670, 1770, and 1860 MPa ultrahigh-strength steel wire for impressed current cathodic protection on cables and hangers. *Int. J. Hydrogen Energy* **2024**, *50*, 1–20. [CrossRef]

Disclaimer/Publisher's Note: The statements, opinions and data contained in all publications are solely those of the individual author(s) and contributor(s) and not of MDPI and/or the editor(s). MDPI and/or the editor(s) disclaim responsibility for any injury to people or property resulting from any ideas, methods, instructions or products referred to in the content.